

The Mean Absorption Line Spectra of a Selection of Luminous $z \sim 6$ Lyman Break Galaxies

Yuichi Harikane^{1,2}, Nicolas Laporte^{3,4}, Richard S. Ellis¹, and Yoshiki Matsuoka⁵

¹ Department of Physics and Astronomy, University College London, Gower Street, London WC1E 6BT, UK

² National Astronomical Observatory of Japan, 2-21-1 Osawa, Mitaka, Tokyo 181-8588, Japan

³ Kavli Institute for Cosmology, University of Cambridge, Madingley Road, Cambridge CB3 0HA, UK

⁴ Cavendish Laboratory, University of Cambridge, 19 JJ Thomson Avenue, Cambridge CB3 0HE, UK and

⁵ Research Center for Space and Cosmic Evolution, Ehime University, Bunkyo-cho, Matsuyama, Ehime 790-8577, Japan

Submitted to ApJ

Abstract

We examine the absorption line spectra of a sample of 31 luminous ($M_{UV} \simeq -23$) Lyman break galaxies at redshift $z \simeq 6$ using data taken with the FOCAS and OSIRIS spectrographs on the Subaru and GTC telescopes. For two of these sources we present longer exposure data taken at higher spectral resolution from ESO's X-shooter spectrograph. Using these data, we demonstrate the practicality of stacking our lower resolution data to measure the depth of various interstellar and stellar absorption lines to probe the covering fraction of low ionization gas and the gas-phase and stellar metallicities near the end of the era of cosmic reionization. From maximum absorption line depths of SiII λ 1260 and CII λ 1334, we infer a mean covering fraction of $\geq 0.85 \pm 0.16$ for our sample. This is larger than that determined using similar methods for lower luminosity galaxies at slightly lower redshifts, suggesting luminous galaxies do not play a prominent role in concluding reionization. Using various interstellar absorption lines we deduce gas-phase metallicities close to solar indicative of substantial early enrichment. Using selected stellar absorption lines, we model our spectra with a range of metallicities using techniques successfully employed at lower redshift and deduce a stellar metallicity of $0.4^{+0.3}_{-0.1}$ solar, consistent with the stellar mass - stellar metallicity relation recently found at $z \sim 3 - 5$. We discuss the implications of these metallicity estimates for the typical ages of our luminous galaxies and conclude our results imply initial star formation at redshifts $z \sim 10$, consistent with independent analyses of earlier objects.

Key words: galaxies: formation — galaxies: evolution — galaxies: high-redshift

1. Introduction

Spectroscopy remains a fundamental tool for understanding the physical processes which govern the evolution of high redshift star-forming galaxies (Stark 2016). Emission line measurements have been effective not only in supplying galaxy redshifts essential for time-slicing deep survey data, but also in interpreting the nature of their radiation field and analyzing gas-phase metallicities (e.g. Erb et al. 2006, Nakajima et al. 2016, Shivaei et al. 2018, Saxena et al. 2019). Although more challenging observationally, absorption line spectroscopy can provide additional physical constraints including evidence of kinematic outflows (Steidel et al. 2010, Jones et al. 2018), the chemistry and ionization state of the interstellar gas (Jones et al. 2012) and, ultimately, stellar metallicities (Leethochawalit et al. 2019, Cullen et al. 2019).

With the exception of studies of rare luminous or gravitationally-lensed examples (e.g. Dow-Hygelund et al. 2005, Jones et al. 2013, Leethochawalit et al. 2016), most progress in absorption line spectroscopy of high redshift galaxies has necessarily involved stacked spectra of representative samples. Following the pioneering study of over 800 Lyman break galaxies (LBGs) at redshift $z \sim 3$ by Shapley et al. (2003), Jones et al. (2012) produced a mean rest-frame UV spectrum utilising 80 LBGs at $z \sim 4$ and, more recently, Cullen et al. 2019 analyzed

composite spectra drawn from a sample of 681 galaxies in the VANDELS survey spanning a range $2.5 < z < 5$ with a mean redshift of $\bar{z} = 3.5$. Redshift-dependent trends in the stacked spectra of LBGs matched in UV luminosity and stellar mass over $2 < z < 4$ based on these earlier campaigns are discussed by Du et al. (2018).

One of the most interesting trends, discussed by both Jones et al. (2013) and Du et al. (2018) is that the equivalent width of low ionization species (LIS) absorption decreases with increasing redshift, possibly due to a reduced covering fraction of neutral hydrogen and, by implication an increased escape fraction, f_{esc} , of ionizing radiation. Reddy et al. (2016) argue that, while the covering fraction of LIS absorption may be a reasonable proxy for that of neutral hydrogen, it may be an unreliable estimate of f_{esc} if metal-enriched outflowing gas has a dust content that varies with the covering fraction of hydrogen. Nonetheless, Du et al. (2018) conclude the evolution of LIS absorption to $z \sim 4$ likely represents an increase in the ionizing capability of higher redshift galaxies with important consequences for cosmic reionization. At redshifts $z < 3$ where the escape fraction can be directly measured, the average for both LBGs and metal-poor Lyman alpha emitters (LAEs) is $f_{\text{esc}} \simeq 5-8\%$ (Steidel et al. 2018, Fletcher et al. 2019). Based on the census of early galaxies, an average $f_{\text{esc}} > 10\%$ is necessary to complete cosmic reionization by $z \simeq 6$ (Robertson et al. 2013). An increase in the average f_{esc} with redshift would thus be

an important result, perhaps indicating earlier galaxies have higher star formation rate surface densities capable of creating porous channels in the interstellar medium (Wise et al. 2014).

Of course it is unlikely that galaxies of different luminosities and stellar masses have similar covering fractions of hydrogen and LIS gas. In this respect to concept of an *average escape fraction* is perhaps naive. Recently there has been much discussion in the literature on the apparent rapidity with which the neutral gas in the intergalactic medium (IGM) became ionized. Estimates of the neutral fraction x_{HI} , including those from the Gunn-Peterson troughs and proximity zones seen in QSO absorption spectra and the fraction of Lyman α emission seen in color-selected $z > 6$ galaxies, collectively imply a rapid evolution from $x_{\text{HI}} \simeq 0.9$ at $z \simeq 7.5$ to zero at $z \simeq 6$ i.e. within a time interval of only 250 Myr (Naidu et al. 2020). Such an abrupt ending of reionization may indicate a contribution of ionizing photons from the rarer, most massive, systems which assemble during at the end of the reionization epoch. The present paper is motivated, in part, to test this hypothesis by examining the absorption spectra of LBGs at a redshift $z \simeq 6$. To date there has been no study at this epoch comparable to those undertaken by the above cited workers at $z \sim 2 - 4$. We present spectra taken with both X-shooter at the ESO Very Large Telescope as well as a sample of 31 galaxies taken with FOCAS and OSIRIS at the Subaru and Gran Telescopio Canarias (GTC) telescopes. We analyze both individual spectra as well as a composite example to determine the nature of LIS features at the highest redshift for which absorption line work is currently practical.

Such absorption line spectra can also be used to examine the *stellar metallicity* of galaxies at high redshift and, particularly, the stellar mass - stellar metallicity relation (Cullen et al. 2019). This is a more attractive, although admittedly more challenging, observational target than that based on gas-phase metallicities, for which there remains debate in the literature about the merits of using local calibrations for the various accessible emission lines, as well as the relative importance of composition and the ionizing radiation field (Steidel et al. 2014). Indeed, gas-phase metallicities beyond redshifts $z \sim 4$ vary widely according to the technique used. Shapley et al. (2017) estimate the metallicity of a luminous galaxy at $z = 4.4$ to be $Z = 0.2Z_{\odot}$ using the $[\text{NeIII}]/[\text{OII}]$ ratio, suggesting a source in the process of enrichment, whereas Faisst et al. (2016) report near solar metallicities at $z \sim 5$ based on empirically calibrated relations between absorption line equivalent widths and metallicities.

A plan of the paper follows. In §2 we discuss the selection of LBGs which form the basis of the present analysis as well as the spectroscopic observations and associated data reduction. In §3 we use a cross-correlation technique to determine the individual redshifts prior to producing composite spectra and their uncertainties. In §4 we discuss our spectra in terms of the covering fraction of LIS absorption and investigate the reliability of using absorption line depths based on our lower resolution Subaru spectra via comparisons with the X-shooter data. We also derive both stellar and interstellar based metallicities and compare these with mass-dependent relationships available at lower redshifts. In §5 we discuss briefly

the implications of our results both for recent models of late cosmic reionization and constraints on the age and earlier enrichment history of our sample.

Throughout this paper we use the recent Planck cosmological parameter sets constrained with the temperature power spectrum, temperature-polarization cross spectrum, polarization power spectrum, low- l polarization, CMB lensing, and external data (TT, TE, EE+lowP+lensing+ext result; Planck Collaboration et al. 2016): $\Omega_{\text{m}} = 0.3089$, $\Omega_{\Lambda} = 0.6911$, $\Omega_{\text{b}} = 0.049$, and $h = 0.6774$. We assume the Salpeter (1955) initial mass function (IMF) with lower and upper mass cutoffs of $0.1 M_{\odot}$ and $100 M_{\odot}$, respectively. All magnitudes are in the AB system (Oke & Gunn 1983), and are corrected for Galactic extinction (Schlegel et al. 1998). The definition of the solar metallicity is given by $12 + \log(\text{O}/\text{H}) = 8.69$ and $Z_{\odot} = 0.0142$ (Asplund et al. 2009).

2. Data

2.1. Galaxy Selection

The galaxies in this study were selected from the Subaru/Hyper Suprime-Cam Subaru strategic program (HSC-SSP) survey datasets (Aihara et al. 2018). The Subaru/HSC survey is a photometric survey with optical broad band filters *grizy* and several narrow-band filters. The survey comprises three layers, UltraDeep, Deep, and Wide, with different combinations of area and depth (see Aihara et al. 2018 for details). LBGs at $z \sim 4 - 7$ are selected from the HSC datasets using the dropout selection technique (Matsuoka et al. 2016, 2018a,b, 2019; Ono et al. 2018; Harikane et al. 2018; Toshikawa et al. 2018), and some of the LBGs have been spectroscopically confirmed (Matsuoka et al. 2016, 2018a,b, 2019; Ono et al. 2018). In this study, we focus on luminous $z \sim 6$ LBGs near the end of the era of cosmic reionization, whose rest-frame UV spectra can be studied with optical spectrographs.

2.2. Spectroscopic Observations

2.2.1. Subaru/FOCAS and GTC/OSIRIS

A total of 31 luminous ($m_y \sim 23 - 24$ mag) galaxies at $z \sim 6$ were spectroscopically confirmed with Subaru/Faint Object Camera and Spectrograph (FOCAS; Kashikawa et al. 2002) and GTC/Optical System for Imaging and low-intermediate-Resolution Integrated Spectroscopy (OSIRIS; Cepa et al. 2000). These spectroscopic data were taken in the SHELLQs program (Matsuoka et al. 2016, 2018a,b, 2019). We will briefly explain the Subaru/FOCAS and GTC/OSIRIS observations and data reduction. Please see the SHELLQs papers (Matsuoka et al. 2016, 2018a,b, 2019) for more details.

The majority of spectra were taken with Subaru/FOCAS observations from 2015 November to 2019 May (IDs: S15B-070, S16B-071I, and S18B-011I; P.I.: Y. Matsuoka). The observations were conducted with the VPH900 grism, SO58 order-sorting filter, and a $1''0$ slit. This configuration provides coverage from $\lambda_{\text{obs}} = 0.75$ to $1.05 \mu\text{m}$ with a spectral resolution of $R \sim 1200$. All the observations were carried out on gray nights with a seeing of $0''.4 - 1''.0$.

Six galaxies were observed with GTC/OSIRIS from 2016 April to 2018 September (GTC19-15B, GTC4-16A, GTC8-17A, GTC3-18A, GTC8-18B, and GTC32-19A;

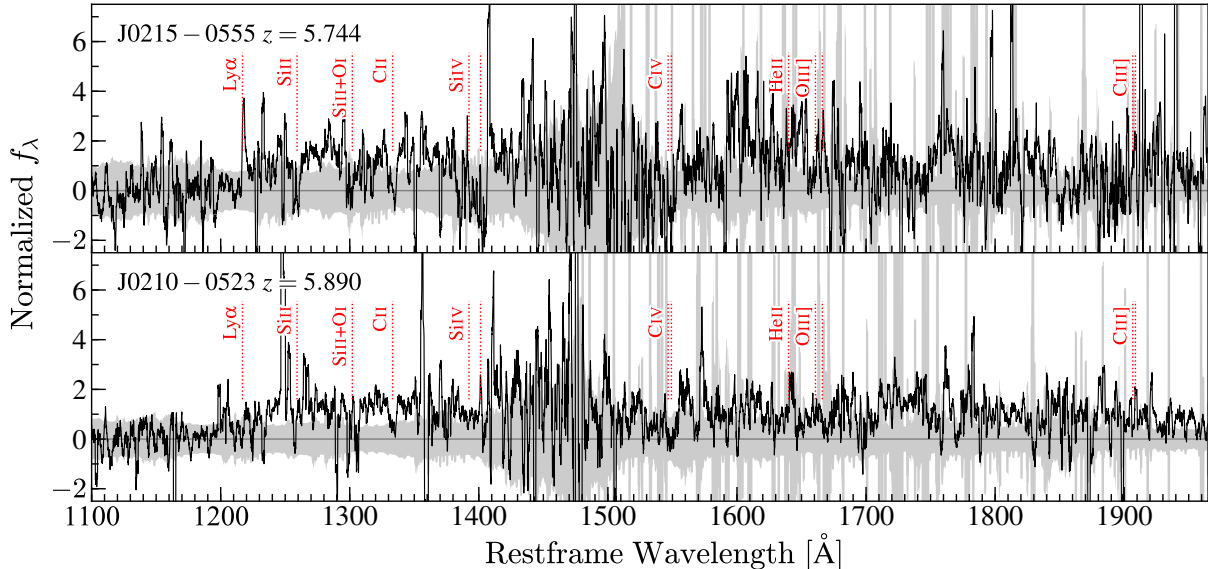


Figure 1. Rest-frame VLT/X-shooter spectra of the targets J0215-0555 and J0210-0523. The gray shaded regions indicate 1σ errors. Key diagnostic emission and absorption lines are indicated with red labels.

PI: K. Iwasawa). These data were taken with the R2500I grism and a $1''$ slit, providing coverage from $\lambda_{\text{obs}} = 0.74$ to $1.05 \mu\text{m}$ with a spectral resolution of $R \sim 1500$. The observations were carried out on both dark and gray nights with a seeing of $0''.6 - 1''.3$.

The FOCAS and OSIRIS exposures are summarized in Table 1. All of the data was reduced using the Image Reduction and Analysis Facility (IRAF). Bias correction, flat fielding with dome flats, sky subtraction, and 1d extraction were performed using standard techniques and wavelength calibration was performed with reference to night sky emission lines. Flux calibration was based on white dwarf or B-type standard stars observed within a few days of the target observations. Slit losses were accounted for by scaling spectra to match the HSC magnitudes.

2.2.2. VLT/X-shooter

Our team was granted 4 half-nights in Visitor Mode in August-September 2017 initially to observe four LBGs among the HSC sample (J0215-0555, J0210-0523, J0219-0416 and J0210-0559, Program 099.A-0128, P.I.: R. Ellis). The planned observing time in each arm was chosen to maximize that in the NIR arm (UVB = 756 sec/exposure, VIS = 819 sec/exposure, and NIR = 900 sec/exposure). We adopted $1.0'' \times 11''$, $0.9'' \times 11''$, and $0.9'' \times 11''$ slits in the UVB, VIS, and NIR arms, respectively. As a result of inclement weather, we concentrated our observations on the two brightest objects, namely J0215-0555¹ ($m_z = 23.8$ mag) and J0210-0523 ($m_z = 24.0$ mag) for which we secured 7.5 hours in good seeing ($< 0.7''$) for each target. Data was reduced using the ESOReflex pipeline (Freudling et al. 2013) version 3.2.0. The rest-frame spectra for these two sources are shown in Figure 1. The systemic redshifts used to produce the rest-frame spectra were measured to be

¹ A fluorescent line $\text{CII}^*1335\text{\AA}$ has been detected in this spectra (see Bosman et al. 2019)

$z = 5.744$ and 5.890 for J0215-0555 and J0210-0523, respectively, following methods presented in Section 3.1. As discussed below, the spectral resolution for these two sources ($R \sim 8000$ in VIS and ~ 6000 in NIR) complements that available for the larger sample of 31 galaxies enabling us to test whether the lower resolution of the FOCAS and OSIRIS spectra is adequate for quantitative absorption line studies.

3. Analysis

3.1. Redshift Determination

In previous studies (Matsuoka et al. 2016, 2018a,b, 2019), provisional redshifts for our 31 galaxies were determined using a variety of tracers including the $\text{Ly}\alpha$ emission line, interstellar absorption lines and the Lyman discontinuity. For the more exacting study of this paper, we secured systemic redshifts for each galaxy in the larger sample based on interstellar absorption lines using the cross-correlation technique (Tonry & Davis 1979). Each spectrum was cross-correlated against the composite spectrum of $80 z \sim 4$ galaxies in Jones et al. (2012) degraded to the appropriate spectral resolution. The same technique was used for the higher resolution X-shooter spectra of J0215-0555 and J0210-0523.

The newly-derived redshifts are presented in Table 1 and typically accurate to $\Delta z < 0.01$. Apart from the velocity offset of $\text{Ly}\alpha$, the results do not significantly differ from those reported in Matsuoka et al. (2016, 2018a,b, 2019). In the specific case of J1211-0118 we adopt $z = 6.0293 \pm 0.0002$ given this is more accurately determined from an ALMA observation (Harikane et al. 2019).

3.2. Composite Spectrum

A composite spectrum of the 31 galaxies studied by FOCAS and OSIRIS was generated by resampling the individual spectra to the rest-frame, normalizing their fluxes to unity, and median stacking. In this way, all individual spectra have equal weight irrespective of the target

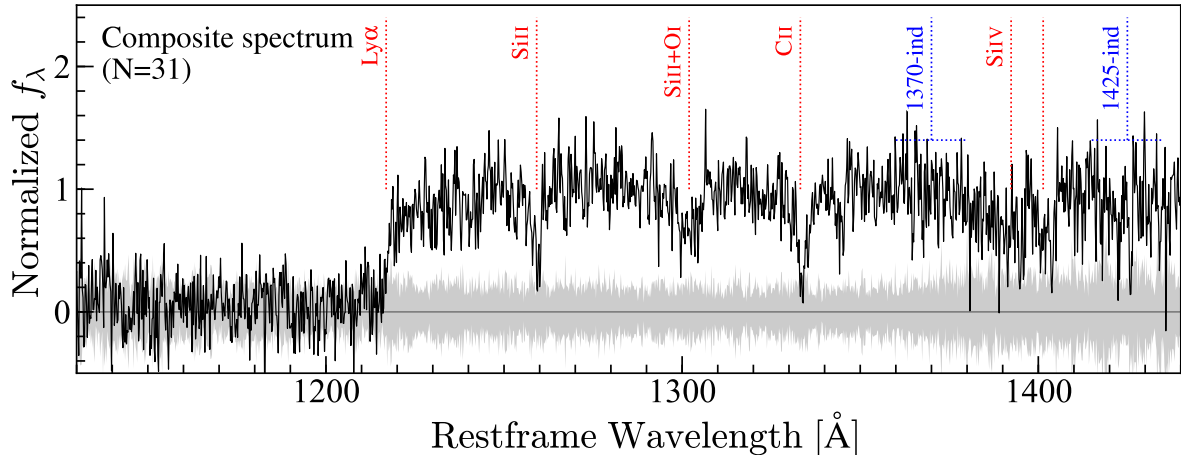


Figure 2. Rest-frame composite spectrum derived from the 31 $z \sim 6$ galaxies studied with FOCAS and OSIRIS. The gray shaded region indicates 1σ uncertainties estimated by bootstrap resampling. Key diagnostic interstellar and stellar absorption features are indicated with red and blue labels, respectively.

brightness or spectral signal/noise. The error spectrum was estimated via bootstrap resampling. We created 100 alternate composites using the same reduced number of spectra drawn at random from the parent sample and adopted an error based upon the standard deviation of these composites. Both the composite and its error are presented in Figure 2. The median redshift and UV luminosities of our sample of $z \sim 6$ galaxies are $z = 5.868$ and $M_{UV} = -22.9$ mag, respectively. Matsuoka et al. (2019) also constructed a composite spectrum of the same 31 galaxies using the provisional redshifts they measured. We note that the equivalent widths (EW) of the absorption lines we analyse in our composite spectrum agree well with their measurements.

4. Results

4.1. Absorption Features

In both the composite spectrum (Figure 2) and individual spectra (Figure 1), we can identify several interstellar absorption lines, including SiII λ 1260, OI λ 1302, SiII λ 1304, CII λ 1334, and SiIV λ 1394,1403. In addition to these interstellar lines, we can also identify an absorption feature near 1425 Å consistent with a blend of stellar photospheric absorption lines arising from metal rich stars (Rix et al. 2004). In the individual X-shooter spectra of J0215-0555 and J0210-0523 that extend the wavelength coverage to longer wavelengths, we identify SiII λ 1260, OI λ 1302, SiII λ 1304, CII λ 1334, SiIV λ 1394,1403, and CIV λ 1548,1550. However, even with the superior spectral resolution, the OI λ 1302 and SiII λ 1204 absorption lines remain blended. Collectively, the presence of these absorption lines indicate that the interstellar media (ISM) of our luminous $z \sim 6$ galaxies are metal enriched, which we discuss in more detail in Section 4.3.

To obtain quantitative measures of these absorption lines, we fit the individual and composite spectra with Gaussian profiles as follows:

$$I(\lambda) = I_0 \exp\left(-\frac{(\lambda - \lambda_0)^2}{2\sigma_\lambda^2}\right) + C, \quad (1)$$

where I_0 , λ_0 , σ_λ , and C are maximum line strength, cen-

tral wavelength, line dispersion, and continuum intensity, respectively. Table 2 presents the resulting absorption line depths, line widths (FWHM) and rest-frame EW. Velocity offsets from the systemic redshift are typically ~ 200 km s $^{-1}$, consistent with the result derived from the $z \sim 4$ composite spectrum (Jones et al. 2012). The absorption line widths are typically ~ 1000 km s $^{-1}$. In Figure 3 we compare our composite spectrum with that derived for the 80 $z \sim 4$ galaxies in Jones et al. (2012). Although the absorption lines at $z \sim 6$ are deeper, we caution that this is not an evolutionary effect because the mean luminosity of the $z \sim 6$ sample is much higher ($M_{UV} \sim -23$ c.f. $M_{UV} \sim -21$ at $z \sim 4$). Several studies have reported larger EWs in more luminous galaxies (e.g., Shapley et al. 2003).

4.2. Covering Fraction

To estimate the neutral gas (HI) covering fraction, we now measure the maximum absorption depth for LIS interstellar absorption lines following the methodology adopted by Jones et al. (2013). Assuming the gas is distributed in a spherical shell, the absorption line profile is related to the covering fraction, f_c , via

$$\frac{I(v)}{C} = 1 - f_c(v)(1 - e^{-\tau(v)}), \quad (2)$$

where C is the continuum intensity defined as the median flux over the wavelength range without absorption lines, and $\tau(v)$ is the optical depth of the relevant absorption line which is related to the column density as

$$\tau(v) = f\lambda \frac{\pi e^2}{m_e c} N(v) = f\lambda \frac{N(v)}{3.768 \times 10^{14}}, \quad (3)$$

where f , λ , and $N(v)$ are the ion oscillator strength, the transition wavelength in Å, and the column density in cm 2 , respectively.

In their study, Jones et al. (2013) used SiII λ 1260, 1304, and 1526 and estimated f_c as a function of velocity for several individual $z \sim 4$ gravitationally-lensed galaxies. They found consistent results despite the different oscillator strengths indicating that the gas is optically thick.

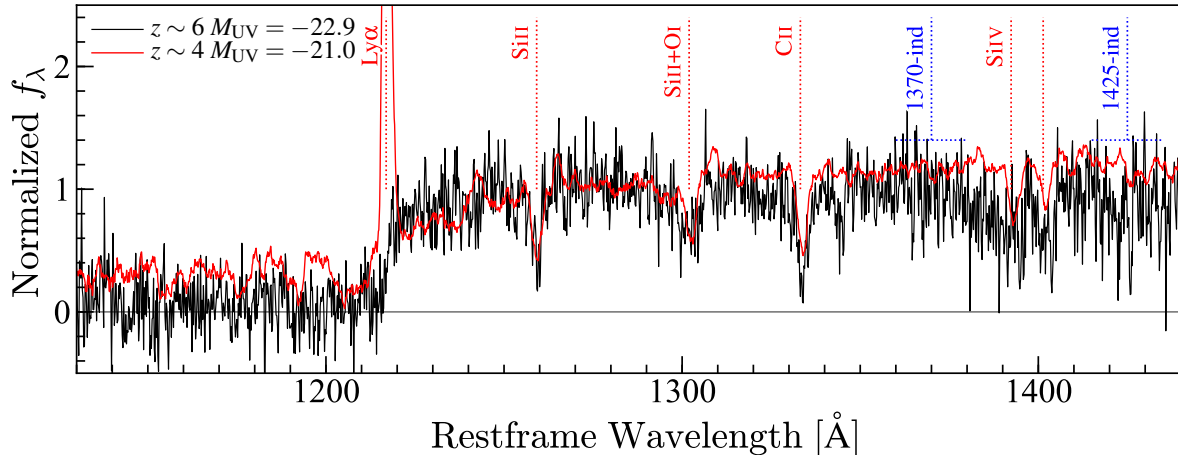


Figure 3. Comparison of the spectrum in Figure 2 (black) with the composite spectrum of 80 $z \sim 4$ galaxies in Jones et al. (2012) (red). The deeper absorption lines in our luminous $z \sim 6$ galaxies indicates an increased low ionization gas covering fraction compared to the less luminous galaxies at $z \sim 4$.

In the optically thick case ($\tau \gg 1$), Equation (2) simplifies to

$$f_c(v) = 1 - \frac{I(v)}{C}. \quad (4)$$

Note that the covering fraction derived in this way formally represents a lower limit.

For the present analysis we constructed the average absorption line profile by calculating a weighted mean of LIS absorption lines as a function of velocity using only SiII λ 1260 and CII λ 1334. We chose not to use OI λ 1302 or SiII λ 1304 transitions because they are heavily blended. Figure 4 shows the averaged absorption line profiles for our $z \sim 6$ composite spectrum, the two X-shooter individual spectra of J0215-0555 and J0210-0523, and the $z \sim 4$ composite in Jones et al. (2012). The estimated maximum absorption line depths are 0.85 ± 0.16 , > 0.40 (2σ), 0.77 ± 0.45 , and 0.57 ± 0.03 for our $z \sim 6$ composite spectrum, J0215-0555, J0210-0523, and the $z \sim 4$ composite spectrum, respectively, as summarized in Table 3. We note that if the systemic redshifts are not measured precisely, the absorption depth in our composite will be underestimated, indicating that true covering fraction could be larger. Finally we note that Jones et al. (2013) examined their average absorption line depths for a subsample based on the prominence of Ly α emission where they found a possible positive correlation. Out of our sample of 31 spectra, only 8 galaxies show prominent Ly α emission (with a median EW of 6.4 Å). We found no significant difference between the absorption line statistics in this stack and that for the larger sample of 23 sources without Ly α emission.

To understand possible systematics in our estimates of the maximum absorption depth based on the lower-resolution FOCAS and OSIRIS spectra, we constructed profiles for the specific cases of J0215-0555 and J0210-0523 and compared these with those based on the higher resolution X-shooter spectra (see red and black lines in Figure 4). We found no significant difference indicating that the resolution of FOCAS ($R \sim 1200$) is sufficient to estimate the maximum absorption line depth largely because of broad line widths involved (typically $\sim 800 - 1000$ km s $^{-1}$). We also degraded the X-shooter

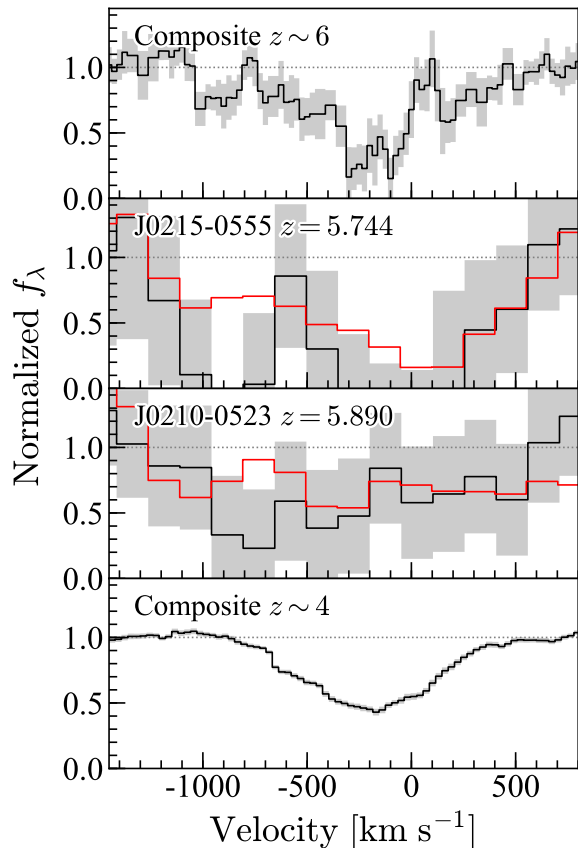


Figure 4. The panels show averaged line profiles (black) with 1σ errors (shaded regions) for (from top to bottom) the $z \sim 6$ composite spectrum, J0215-0555, J0210-0523, and the $z \sim 4$ composite spectrum in Jones et al. (2012). The black and red lines for the panels of J0215-0555 and J0210-0523 represent profiles derived from the X-shooter and FOCAS data, respectively.

spectra to the lower resolution appropriate for the FOCAS/OSIRIS composite and similarly found no change in the absorption line depth.

In Figure 5, we plot the estimated maximum absorp-

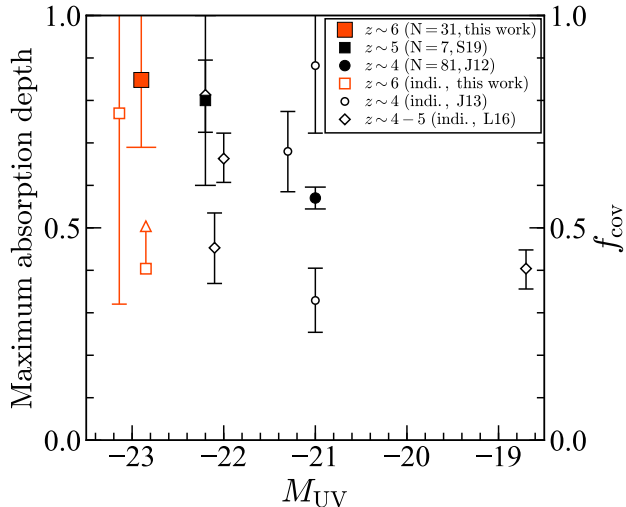


Figure 5. Maximum absorption depth as a function of UV luminosity drawn from our $z \sim 6$ composite spectrum (red filled square), J0215-0555 and J0210-0523 (open red square), composites at $z \sim 5$ and ~ 4 in Sugahara et al. (2019) and Jones et al. (2012), respectively (black filled symbols), and individual galaxies in Jones et al. (2013) and Leethochawalit et al. (2016) (black open symbols).

tion depth as a function of the UV luminosity. As discussed earlier, the maximum absorption depth of our $z \sim 6$ galaxies is larger than those of less luminous sources at $z \sim 4 - 5$ (Jones et al. 2012, 2013; Leethochawalit et al. 2016; Sugahara et al. 2019). This should not be interpreted as an evolutionary trend given the significantly different luminosities. The major implication is for a higher covering fraction of low ionization gas for our sample of $z \sim 6$ luminous galaxies and thus a lower typical ionizing photon escape fraction.

4.3. Gas-phase metallicity

Since the rest-frame optical emission lines normally used to estimate gas-phase metallicities are redshifted to the mid-infrared beyond reach of ground-based telescopes, we can only use empirically-calibrated relations between the oxygen abundance and interstellar absorption line measures (Faisst et al. 2016). For this measure, we use the $\text{OII}\lambda 1302 + \text{SiII}\lambda 1304$ complex (referred to as the $\text{SiII}\lambda 1300$ complex in Faisst et al. 2016), $\text{CII}\lambda 1334$, $\text{SiIV}\lambda 1394, 1403$, and $\text{CIV}\lambda 1548, 1550$ (only for the X-shooter spectra). We use the best-fit parameters in Faisst et al. (2016), but an uncertainty of assuming the best-fit parameters is much smaller than the statistical errors. In this way, we find gas-phase metallicities close to solar values. Specifically, $12 + \log(\text{O}/\text{H}) = 8.7_{-0.2}^{+0.1}$, $9.2_{-0.4}^{+0.4}$, and $8.6_{-0.6}^{+0.4}$ ($Z_{\text{gas}} = 1.0_{-0.4}^{+0.3}$, $3.2_{-2.0}^{+4.9}$, and $0.8_{-0.6}^{+1.2} Z_{\odot}$) for the $z \sim 6$ composite spectrum, J0215-0555, and J0210-0523, respectively, as summarized in Table 3.

In Figure 6, we plot these gas-phase metallicities as a function of stellar mass where, in absence of Spitzer photometry, we derive approximate stellar masses based on an empirical relation with the UV luminosity given in Song et al. (2016). The resulting relation shows that our galaxies have metallicities comparable to those at the massive end of the $z \sim 0$ mass-metallicity relation in Curti et al. (2020) and are already metal-enriched. Although these measures are comparable with those of

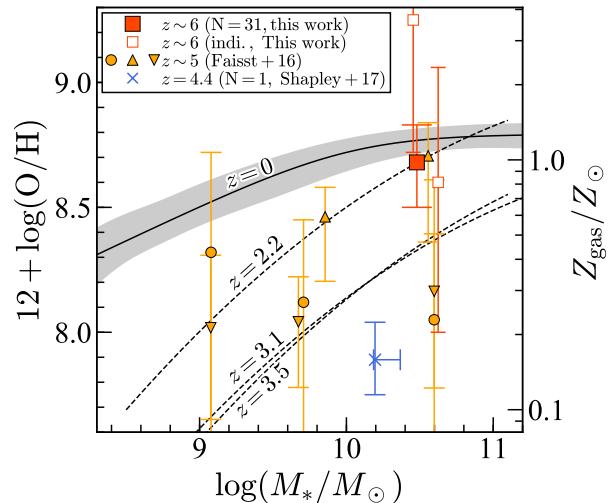


Figure 6. Gas-phase metallicity as a function of the stellar mass based upon the $z \sim 6$ composite spectrum and two individual spectra (J0215-0555 and J0210-0523, red filled and open squares), $z \sim 5$ galaxies in Faisst et al. (2016) (orange symbols where circles, upward triangles, and downward triangles refer to all galaxies, those with weak/no $\text{Ly}\alpha$, and with $\text{Ly}\alpha$, respectively). The blue cross represents a galaxy at $z = 4.4$ in Shapley et al. (2017). For comparison, we plot relations at $z = 0$ (Curti et al. 2020), $z = 2.2$, 3.5 (Maiolino et al. 2008), and $z = 3.1$ (Mannucci et al. 2009).

$z \sim 5$ galaxies with weak/no $\text{Ly}\alpha$ emission (Faisst et al. 2016), they lie above mass metallicity relations at $z = 3.1$ and 3.5 in Maiolino et al. (2008) and Mannucci et al. (2009) which seems surprising. However, Nakajima & Ouchi (2014) point out that the published metallicities at $z = 3.1 - 3.5$ would be higher if the assumed ionization parameter was closer to more recent estimates (e.g., Nakajima et al. 2013; Nakajima & Ouchi 2014; Harikane et al. 2019). Future JWST rest-frame optical spectroscopy for a large sample of high redshift galaxies will resolve this issue and securely determine the gas-phase metallicities and the mass-metallicity relation of high redshift galaxies.

4.4. Stellar metallicity

In our composite spectrum, we identify a significant feature near 1425 \AA which arises from photospheric absorption associated with stellar winds in massive stars. Its absorption line strength (and that of the blend near 1370 and 1425 \AA ; the ‘1370’ and ‘1425’ indices) have been used as indicator of stellar metallicity (Leitherer et al. 2001; Rix et al. 2004).

To evaluate the possibilities, we compared our observed composite spectrum with model spectra assuming different metallicities following the techniques described by Steidel et al. (2016) and Cullen et al. (2019). By simulating the entire spectrum, we can also use additional weaker features. For our model spectra we ran BPASSv2² (Eldridge & Stanway 2016; Stanway et al. 2016) sampling metallicities over a grid of $Z_* = (0.001, 0.002, 0.003, 0.004, 0.006, 0.008, 0.010, 0.014)$, adopting the Salpeter (1955) IMF including binary stars and a continuous star formation history with a

² <https://bpass.auckland.ac.nz/>

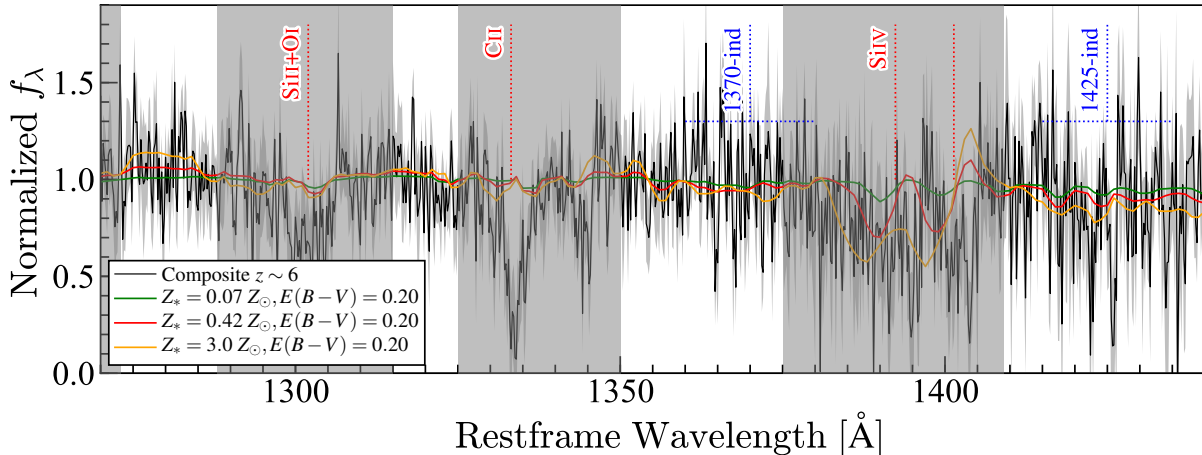


Figure 7. Estimating the stellar metallicity at $z \sim 6$. The black line represents the $z \sim 6$ composite spectrum and grey shaded regions indicate masked wavelength ranges not used for fitting because of the prominent interstellar absorption lines. Green, red and orange curves represent BPASS model spectra (see text for details) with stellar metallicities of $Z_* = 0.07$, 0.42 , and $3.0 Z_\odot$, respectively, and a color excess of $E(B - V) = 0.20$. Absorption features near 1370 and 1425 \AA become deeper with higher metallicities.

duration of 100 Myr .³ As these models do not include the nebular continuum, we calculated the additional contribution using Cloudy (Ferland et al. 1998, 2017) version 17.01. Assuming typical high redshift values for the electron density $n_e = 300 \text{ cm}^{-3}$ and ionization parameter $\log U = -2.8$ (Steidel et al. 2016), this contributes an additional 10% to the total far-UV continuum. The resulting model spectra were reddened following the Calzetti et al. (2000) dust extinction law parameterized by a color excess in the range of $0.00 \leq E(B - V) \leq 1.00$, and IGM attenuation applied following the approach given by Inoue et al. (2014). Figure 7 shows a selection of models with $Z = 0.07$, 0.42 , and $3.0 Z_\odot$ with $E(B - V) = 0.20$ alongside our composite spectrum.

To determine the best model, we calculated χ^2 value for each model following

$$\chi^2 = \sum_i \left(\frac{f_i^{\text{model}} - f_i^{\text{obs}}}{\sigma_i} \right)^2, \quad (5)$$

where f_i^{obs} and σ_i are the observed flux and its error at each wavelength, and f_i^{model} is the model spectrum normalized to the observed continuum level. The fit was confined to wavelength ranges of $1273 < \lambda/\text{\AA} < 1288$, $1315 < \lambda/\text{\AA} < 1325$, $1350 < \lambda/\text{\AA} < 1375$, and $1409 < \lambda/\text{\AA} < 1440$ which include absorption features near 1370 and 1425 \AA and avoid interstellar features. Our best-fit stellar metallicity and color excess are, respectively, $Z_* = 0.42^{+0.28}_{-0.14} Z_\odot$ and $E(B - V) = 0.20^{+0.06}_{-0.07}$ with a reduced χ^2 value of $\chi^2/\nu = 0.97$ (see Table 3 and the red curve in Figure 7).

In Figure 8, we plot our estimated stellar metallicity as a function of the stellar mass. It can be seen that, for our $z \sim 6$ luminous galaxies, our result agrees with an extrapolation of the mass-metallicity relation at $z \sim 3 - 5$

³ Assuming a shorter duration of 10 Myr does not change the conclusions, and assuming an older age does not affect our results because the photospheric absorption line EWs near 1370 and 1425 \AA are saturated at $> 30 \text{ Myr}$ (Rix et al. 2004)

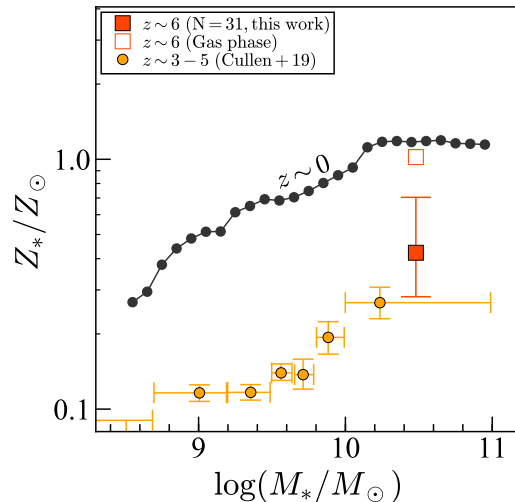


Figure 8. Stellar metallicity as a function of the stellar mass based upon our $z \sim 6$ galaxies (red filled square), $z \sim 3 - 5$ galaxies from Cullen et al. (2019) and $z \sim 0$ from Zahid et al. (2017) (orange and black circles respectively). The red open square represents the gas-phase metallicity based upon our $z \sim 6$ galaxies (see Figure 6).

from VANDELS in Cullen et al. (2019) and is significantly lower than the $z \sim 0$ relation (Zahid et al. 2017). Importantly, our stellar metallicity is lower than the gas-phase metallicity estimated in Section 4.3. We return to discuss this difference in Section 5.2.

4.5. Emission Lines

The X-shooter spectra cover the near-infrared wavelength region where, at high redshift, important rest-frame UV emission lines such as $\text{HeII}\lambda 1640$, $\text{OIII}\lambda\lambda 1661, 1666$, $[\text{CIII}]\lambda 1907$, and $\text{CIII}\lambda 1909$ might be visible. We do not detect any of these emission lines with typical 3σ upper limits of the rest-frame EW of $< 0.5 \text{ \AA}$. These non-detections are consistent with published trends for weaker emission in more luminous galaxies (e.g., Shapley et al. 2003; Shibuya et al. 2018). Since some of these lines are seen in metal-poor galaxies (e.g.,

Berg et al. 2018; Nakajima et al. 2018), this provides further evidence that our $z \sim 6$ galaxies are metal-enriched.

5. Discussion

5.1. Implication for Reionization

We find that the average low ionization gas covering fractions for our luminous $z \sim 6$ galaxies is significant, $f_c \geq 0.85 \pm 0.16$, and, as shown in Figure 5, this largely arises due to a luminosity dependence. Given the expected inverse relationship with respect to the ionizing photon escape fraction, i.e. $f_{\text{esc}} \simeq 1 - f_c$, and the fact the ionizing photon production efficiency for LBGs, ξ_{ion} , does not depend strongly on UV luminosity (e.g., Bouwens et al. 2016), our result implies luminous $z \sim 6$ galaxies are not dominant contributors to concluding cosmic reionization, as we discuss further below.

Recently, there has been much interest in the suggestion that galaxies of various luminosities made distinct contributions to the reionization process due, for example, to differing escape fractions or ionizing photon production rates. This contrasts with early articles (e.g. Robertson et al. 2013, 2015) which assumed a constant f_{esc} and ξ_{ion} independent of luminosity so that the process was governed by the most abundant, low-luminosity, sources. Even so, a high average fraction, $f_{\text{esc}} \simeq 0.2$, was deemed necessary to complete reionization by $z \simeq 6$.

To resolve this possible ‘ionizing photon deficit’, Finkelstein et al. (2019) presented a model where the escape fraction is significantly higher in less luminous galaxies on the basis of simulations conducted by Paardekooper et al. (2015). In this model, $\sim 80\%$ of the ionizing budget arises from sub-luminous galaxies with $M_{\text{UV}} > -16$ mag. While possibly consistent with the present paper’s results, Finkelstein’s model predicts a relatively smooth evolution of the IGM neutral hydrogen fraction, e.g., $x_{\text{HI}} = 0.3$ at $z = 7.5$, which seems in tension with measures of QSO damping wings and Ly α fractions, $x_{\text{HI}} \simeq 0.4 - 0.9$ (Bolton et al. 2011; Bañados et al. 2018; Mason et al. 2018, 2019; Hoag et al. 2019), as mentioned in Finkelstein et al. (2019) and Naidu et al. (2020).

The apparent rapid evolution of x_{HI} over $6 < z < 7.5$ led Naidu et al. (2020) to propose an alternative model where late reionization is governed by the most luminous galaxies with high star formation rate surface densities, Σ_{SFR} . Adopting a relationship whereby $f_{\text{esc}} \propto \Sigma_{\text{SFR}}^{0.4}$, $\gtrsim 80\%$ of the ionizing budget is contributed by luminous galaxies with $M_{\text{UV}} < -18$ mag, and the abrupt end of the reionization process as indicated by Gunn-Peterson troughs, QSO damping wings and Ly α fractions can be reconciled. The large covering fractions we find for the most luminous $z \sim 6$ galaxies seems to provide little support for such a model.

Ultimately, progress in addressing the relative roles of galaxies of different luminosities will depend on the accuracy of the various measures of the IGM neutral fraction, x_{HI} . Finkelstein et al. (2019) discuss several reasons to be cautious when interpreting QSO damping wing and Ly α fraction data, because the derived x_{HI} measurements are very model dependent. If, as we suggest, escape fractions are indeed lower in luminous galaxies, the validity of current measures of x_{HI} may need to be re-considered.

5.2. Enhanced O/Fe ratio

We find that the gas-phase metallicity estimated from our $z \sim 6$ composite spectrum, $Z_{\text{gas}} \simeq 1.0 Z_{\odot}$, is higher than the stellar metallicity, $Z_{*} \simeq 0.4 Z_{\odot}$. Such a difference is also seen in lower redshift galaxies (Steidel et al. 2016; Cullen et al. 2019). We note that the empirical relations used to estimate the gas-phase metallicity is calibrated with the oxygen abundance, $12 + \log(\text{O}/\text{H})$, whereas the stellar metallicity is estimated from photospheric absorption in the rest-UV continuum dominated mainly by iron-peak element (Steidel et al. 2016). Accordingly the difference between gas-phase and stellar metallicities indicates a non-solar elemental abundance pattern, i.e., a super-solar O/Fe ratio.⁴ From our two metallicity estimates in the $z \sim 6$ composite spectrum, we derive an O/Fe ratio of $(\text{O}/\text{Fe}) \simeq 2.4 \times (\text{O}/\text{Fe})_{\odot}$. Such super-solar O/Fe ratios have also been reported at lower redshifts; $(\text{O}/\text{Fe}) \sim 3 - 7 \times (\text{O}/\text{Fe})_{\odot}$ at $z \sim 2$ (Steidel et al. 2016; Strom et al. 2018; Topping et al. 2019) and $(\text{O}/\text{Fe}) \gtrsim 1.8 \times (\text{O}/\text{Fe})_{\odot}$ at $z \sim 3 - 5$ (Cullen et al. 2019).

A super-solar O/Fe ratio is not surprising for galaxies whose ISM has been enriched primarily by Type II (core-collapse) supernovae (SNe). Oxygen is a primary product of core-collapse SNe and therefore has a short formation timescale, while iron production occurs largely from Type Ia SNe which form ~ 1 Gyr after star formation (Figure 1 in Maiolino & Mannucci 2019). Quantitatively, the yield from core-collapse SNe is a super-solar O/Fe ratio; $(\text{O}/\text{Fe}) \sim 4 - 6 \times (\text{O}/\text{Fe})_{\odot}$ for the Salpeter (1955) IMF (Nomoto et al. 2006), $\sim 3 \times (\text{O}/\text{Fe})_{\odot}$ for the Kroupa (2001) IMF (Chieffi & Limongi 2004; Limongi & Chieffi 2006). By contrast, the yield from Type Ia SNe is $(\text{O}/\text{Fe}) \sim 0.03 \times (\text{O}/\text{Fe})_{\odot}$ (Iwamoto et al. 1999). For our $z \sim 6$ galaxies, seen ~ 1 Gyr after the Big Bang, metal enrichment is therefore dominated by core-collapse SNe with yields of $(\text{O}/\text{Fe}) \sim 3 - 6 \times (\text{O}/\text{Fe})_{\odot}$.

5.3. Implication for star formation prior to $z \sim 6$

The near-solar gas-phase metallicity we observe for our $z \sim 6$ galaxies is higher than that predicted by recent theoretical simulations. For example, the IllustrisTNG simulation predicts a gas-phase metallicity of $Z_{\text{gas}} \simeq 0.4 - 0.5 Z_{\odot}$ for massive galaxies at $z = 6$ with $\log(M_{*}/M_{\odot}) = 10.5$ (Torrey et al. 2019). Although the FIRE simulation predicts the $z = 6$ mass-metallicity relation only to masses of $\log(M_{*}/M_{\odot}) = 9.5$ (Ma et al. 2016), extrapolating the relation still implies $Z_{\text{gas}} \sim 0.3 Z_{\odot}$ at $\log(M_{*}/M_{\odot}) = 10.5$. As discussed in Cullen et al. (2019), these simulations suffer from uncertainties in the assumed stellar yields, the strength of galactic outflows and star formation histories. The higher metallicities we observe may imply star formation began much earlier than predicted in the simulations.

To quantify the possibility of star formation prior to $z \sim 6$, we compare our results with the analytic one-zone chemical evolution model presented in Weinberg et al. (2017, hereafter W17). In this model, gas is enriched from both core-collapse and Type Ia SNe with yields given by Chieffi & Limongi (2004), Limongi &

⁴ It is safe to assume that gas-phase and stellar metallicities trace similar timescales because our stellar metallicity is estimated from the rest-UV spectrum dominated by short-lived massive stars.

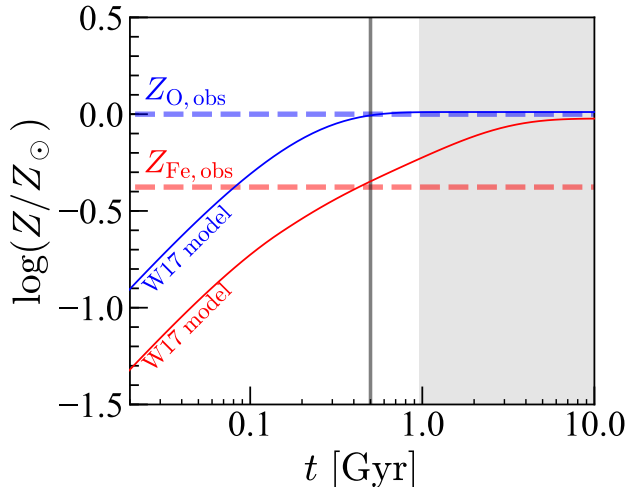


Figure 9. The metallicity predicted in the chemical evolution model of Weinberg et al. (2017, W17) as a function of time after initial star formation. Blue and red solid curves represent predicted oxygen and iron abundances assuming a constant star formation history with a gas depletion timescale of $t_{\text{dep}} = 400$ Myr and the mass loading factor of $\eta = 2$. Horizontal dashed lines indicate the observed gas-phase (oxygen) and stellar (iron) metallicities for our $z \sim 6$ composite. Continuous star formation over ~ 500 Myr is required to reproduce the observed metallicities. The gray-shaded region defines the parameter space rejected by the finite cosmic age at $z \sim 6$ (~ 1 Gyr).

Chieffi (2006), and Iwamoto et al. (1999). Type Ia SNe suffer a minimum delay time of 0.15 Gyr and an e -folding timescale of 1.5 Gyr that are fiducial values in W17. The star formation rate (SFR) is coupled to the gas mass (M_{gas}) with a gas depletion timescale, $t_{\text{dep}} = M_{\text{gas}}/SFR$, assumed to be constant. Here we adopt $t_{\text{dep}} = 400$ Myr following the prescription of Scoville et al. (2017) at $z = 6$. The gas outflow is assumed to be a constant multiple of the SFR with a mass-loading factor of $\eta = \dot{M}_{\text{out}}/SFR$, where we assume $\eta = 2$ (we discuss the sensitivity to this choice below). The case for three star formation histories are explicitly solved in W17, but here we consider the constant star formation history for illustrative purposes.

Figure 9 shows the evolving abundances as a function of time from initial star formation. The oxygen abundance rapidly reaches a solar value in ~ 500 Myr whereas for the iron abundance this takes > 1 Gyr. To reproduce the observed values in the case of a constant SFR we need a stellar age of 500 Myr. Decreasing η pushes metal enrichment to earlier epochs, but a constant SFR is still needed over a duration of ~ 200 Myr even for the case of zero outflow ($\eta = 0$). While uncertainties remain, the metallicities we observe in our $z \sim 6$ galaxies indicate enrichment that began up to 500 Myr prior to $z \sim 6$, corresponding to a formation redshift $z \sim 10$, consistent with that implied by mature stellar populations inferred in higher redshift galaxies (Hashimoto et al. 2018; Roberts-Borsani et al. 2020).

6. Summary

We examine the absorption line spectra of a sample of 31 luminous Lyman break galaxies at redshift $z \sim 6$ selected from the Subaru/Hyper Suprime-Cam Subaru strategic program for which spectra were taken using

the Subaru/FOCAS and GTC/OSIRIS spectrographs. For two individual sources we present longer exposure data taken at higher spectral resolution with VLT/X-shooter. Using these data, we demonstrate the practicality of stacking our lower resolution data to measure the depth of absorption lines and thereby to probe both the covering fraction of low ionization gas and the mean gas-phase and stellar metallicity near the end of cosmic reionization. Our major findings are summarized below.

1. We identify interstellar absorption lines of SiII, OI, CII, and SiIV in the composite and individual spectra of our $z \sim 6$ galaxies. These absorption lines are deep and broad, typically with EWs of $\sim 2-3 \text{ \AA}$ and line widths of $\sim 1000 \text{ km s}^{-1}$. As a result of these broad absorption lines, we verify using our higher resolution X-shooter spectra that the spectral resolution of the FOCAS and OSIRIS data is sufficient to reliably estimate the depth of absorption.
2. We find a maximum absorption depth of 0.85 ± 0.16 in the composite spectrum of our luminous ($M_{\text{UV}} \sim -23$ mag) galaxies. This is deeper than that of less luminous ($M_{\text{UV}} \sim -21$ mag) galaxies at $z \sim 4$ and indicates a higher gas covering fraction and, by implication, a lower ionizing photon escape fraction. Our result at $z \sim 6$ contrasts with the suggestion by Naidu et al. (2020) that the most luminous galaxies must play a key role to ensure a rapid conclusion to cosmic reionization. Our result tends to support earlier models where the bulk of the ionizing photons arise from lower luminosity galaxies (e.g. Robertson et al. 2013, 2015, Finkelstein et al. 2019). Since the predictions from these models in tension with model-dependent measurements of the neutral fraction based on the damping wing in QSO spectra and the incidence of Ly α emission in color-selected galaxies, it is important to understand the accuracy of such measures.
3. We estimate the gas-phase metallicity of our galaxies using empirical relations linking these to the EWs of interstellar absorption lines. We find abundances close to solar, indicating that our luminous galaxies are already metal enriched at $z \sim 6$. Similarly, we estimate a lower stellar metallicity of ~ 0.4 solar, which we interpret in terms of a super-solar O/Fe ratio given the stellar and gas-phase metallicities trace different elements enriched by core-collapse SNe. A comparison with the one-zone chemical evolution model in Weinberg et al. (2017) indicates that metal enrichment in our $z \sim 6$ galaxies began up to 500 Myr prior to $z \sim 6$, corresponding to a formation redshift $z \sim 10$.

Our study provides a valuable impetus for more detailed absorption line studies of individual $z > 6$ galaxies which will become practical with the James Webb Space Telescope.

We thank Tucker Jones for sending us his composite $z \sim 4$ spectrum, Andreas Faisst for providing parameter sets in his Monte Carlo simulations, and acknowledge useful discussions with Aayush Saxena. YH

acknowledges support from the JSPS KAKENHI grant No. 19J01222 through the JSPS Research Fellowship for Young Scientists. RSE acknowledges funding from the European Research Council (ERC) under the European Union's Horizon 2020 research and innovation programme (grant agreement No 669253). NL acknowledges financial support from the Kavli Foundation.

REFERENCES

- Aihara, H., Arimoto, N., Armstrong, R., et al. 2018, *PASJ*, 70, S4
 Asplund, M., Grevesse, N., Sauval, A. J., & Scott, P. 2009, *ARA&A*, 47, 481
 Bañados, E., Venemans, B. P., Mazzucchelli, C., et al. 2018, *Nature*, 553, 473
 Berg, D. A., Erb, D. K., Auger, M. W., Pettini, M., & Brammer, G. B. 2018, *ApJ*, 859, 164
 Bolton, J. S., Haehnelt, M. G., Warren, S. J., et al. 2011, *MNRAS*, 416, L70
 Bosman, S. E. I., Laporte, N., Ellis, R. S., Ouchi, M., & Harikane, Y. 2019, *MNRAS*, 487, L67
 Bouwens, R. J., Smit, R., Labbé, I., et al. 2016, *ApJ*, 831, 176
 Calzetti, D., Armus, L., Bohlin, R. C., et al. 2000, *ApJ*, 533, 682
 Cepa, J., Aguiar, M., Escalera, V. G., et al. 2000, Society of Photo-Optical Instrumentation Engineers (SPIE) Conference Series, Vol. 4008, OSIRIS tunable imager and spectrograph, ed. M. Iye & A. F. Moorwood, 623–631
 Chieffi, A., & Limongi, M. 2004, *ApJ*, 608, 405
 Cullen, F., McLure, R. J., Dunlop, J. S., et al. 2019, *MNRAS*, 487, 2038
 Curti, M., Mannucci, F., Cresci, G., & Maiolino, R. 2020, *MNRAS*, 491, 944
 Dow-Hygelund, C. C., Holden, B. P., Bouwens, R. J., et al. 2005, *ApJ*, 630, L137
 Du, X., Shapley, A. E., Reddy, N. A., et al. 2018, *ApJ*, 860, 75
 Eldridge, J. J., & Stanway, E. R. 2016, *MNRAS*, 462, 3302
 Erb, D. K., Shapley, A. E., Pettini, M., et al. 2006, *ApJ*, 644, 813
 Faist, A. L., Capak, P. L., Davidzon, I., et al. 2016, *ApJ*, 822, 29
 Ferland, G. J., Korista, K. T., Verner, D. A., et al. 1998, *PASP*, 110, 761
 Ferland, G. J., Chatzikos, M., Guzmán, F., et al. 2017, *Rev. Mexicana Astron. Astrofis.*, 53, 385
 Finkelstein, S. L., D’Aloisio, A., Paardekooper, J.-P., et al. 2019, *ApJ*, 879, 36
 Fletcher, T. J., Tang, M., Robertson, B. E., et al. 2019, *ApJ*, 878, 87
 Freudling, W., Romaniello, M., Bramich, D. M., et al. 2013, *A&A*, 559, A96
 Harikane, Y., Ouchi, M., Ono, Y., et al. 2018, *PASJ*, 70, S11
 Harikane, Y., Ouchi, M., Inoue, A. K., et al. 2019, arXiv e-prints, arXiv:1910.10927
 Hashimoto, T., Laporte, N., Mawatari, K., et al. 2018, *Nature*, 557, 392
 Hoag, A., Bradač, M., Huang, K., et al. 2019, *ApJ*, 878, 12
 Inoue, A. K., Shimizu, I., Iwata, I., & Tanaka, M. 2014, *MNRAS*, 442, 1805
 Iwamoto, K., Brachwitz, F., Nomoto, K., et al. 1999, *ApJS*, 125, 439
 Jones, T., Stark, D. P., & Ellis, R. S. 2012, *ApJ*, 751, 51
 —. 2018, *ApJ*, 863, 191
 Jones, T. A., Ellis, R. S., Schenker, M. A., & Stark, D. P. 2013, *ApJ*, 779, 52
 Kashikawa, N., Aoki, K., Asai, R., et al. 2002, *PASJ*, 54, 819
 Kroupa, P. 2001, *MNRAS*, 322, 231
 Leethochawalit, N., Jones, T. A., Ellis, R. S., Stark, D. P., & Zitrin, A. 2016, *ApJ*, 831, 152
 Leethochawalit, N., Kirby, E. N., Ellis, R. S., Moran, S. M., & Treu, T. 2019, *ApJ*, 885, 100
 Leitherer, C., Leão, J. R. S., Heckman, T. M., et al. 2001, *ApJ*, 550, 724
 Limongi, M., & Chieffi, A. 2006, *ApJ*, 647, 483
 Ma, X., Hopkins, P. F., Faucher-Giguère, C.-A., et al. 2016, *MNRAS*, 456, 2140
 Maiolino, R., & Mannucci, F. 2019, *A&A Rev.*, 27, 3
 Maiolino, R., Nagao, T., Grazian, A., et al. 2008, *A&A*, 488, 463
 Mannucci, F., Cresci, G., Maiolino, R., et al. 2009, *MNRAS*, 398, 1915
 Mason, C. A., Treu, T., Dijkstra, M., et al. 2018, *ApJ*, 856, 2
 Mason, C. A., Fontana, A., Treu, T., et al. 2019, *MNRAS*, 485, 3947
 Matsuoka, Y., Onoue, M., Kashikawa, N., et al. 2016, *ApJ*, 828, 26
 —. 2018a, *PASJ*, 70, S35
 Matsuoka, Y., Iwasawa, K., Onoue, M., et al. 2018b, *ApJS*, 237, 5
 —. 2019, *ApJ*, 883, 183
 Naidu, R. P., Tacchella, S., Mason, C. A., et al. 2020, *ApJ*, 892, 109
 Nakajima, K., Ellis, R. S., Iwata, I., et al. 2016, *ApJ*, 831, L9
 Nakajima, K., & Ouchi, M. 2014, *MNRAS*, 442, 900
 Nakajima, K., Ouchi, M., Shimasaku, K., et al. 2013, *ApJ*, 769, 3
 Nakajima, K., Schaerer, D., Le Fèvre, O., et al. 2018, *A&A*, 612, A94
 Nomoto, K., Tominaga, N., Umeda, H., Kobayashi, C., & Maeda, K. 2006, *Nucl. Phys. A*, 777, 424
 Oke, J. B., & Gunn, J. E. 1983, *ApJ*, 266, 713
 Ono, Y., Ouchi, M., Harikane, Y., et al. 2018, *PASJ*, 70, S10
 Paardekooper, J.-P., Khochfar, S., & Dalla Vecchia, C. 2015, *MNRAS*, 451, 2544
 Planck Collaboration, Ade, P. A. R., Aghanim, N., et al. 2016, *A&A*, 594, A13
 Reddy, N. A., Steidel, C. C., Pettini, M., Bogosavljević, M., & Shapley, A. E. 2016, *ApJ*, 828, 108
 Rix, S. A., Pettini, M., Leitherer, C., et al. 2004, *ApJ*, 615, 98
 Roberts-Borsani, G., Ellis, R. S., & Laporte, N. 2020, arXiv e-prints, arXiv:2002.02968
 Robertson, B. E., Ellis, R. S., Furlanetto, S. R., & Dunlop, J. S. 2015, *ApJ*, 802, L19
 Robertson, B. E., Furlanetto, S. R., Schneider, E., et al. 2013, *ApJ*, 768, 71
 Salpeter, E. E. 1955, *ApJ*, 121, 161
 Saxena, A., Pentericci, L., Mirabelli, M., et al. 2019, arXiv e-prints, arXiv:1911.09999
 Schlegel, D. J., Finkbeiner, D. P., & Davis, M. 1998, *ApJ*, 500, 525
 Scoville, N., Lee, N., Vanden Bout, P., et al. 2017, *ApJ*, 837, 150
 Shapley, A. E., Steidel, C. C., Pettini, M., & Adelberger, K. L. 2003, *ApJ*, 588, 65
 Shapley, A. E., Sanders, R. L., Reddy, N. A., et al. 2017, *ApJ*, 846, L30
 Shibuya, T., Ouchi, M., Harikane, Y., et al. 2018, *PASJ*, 70, S15
 Shivaee, I., Reddy, N. A., Siana, B., et al. 2018, *ApJ*, 855, 42
 Song, M., Finkelstein, S. L., Ashby, M. L. N., et al. 2016, *ApJ*, 825, 5
 Stanway, E. R., Eldridge, J. J., & Becker, G. D. 2016, *MNRAS*, 456, 485
 Stark, D. P. 2016, *ARA&A*, 54, 761
 Steidel, C. C., Bogosavljević, M., Shapley, A. E., et al. 2018, *ApJ*, 869, 123
 Steidel, C. C., Erb, D. K., Shapley, A. E., et al. 2010, *ApJ*, 717, 289
 Steidel, C. C., Strom, A. L., Pettini, M., et al. 2016, *ApJ*, 826, 159
 Steidel, C. C., Rudie, G. C., Strom, A. L., et al. 2014, *ApJ*, 795, 165
 Strom, A. L., Steidel, C. C., Rudie, G. C., Trainor, R. F., & Pettini, M. 2018, *ApJ*, 868, 117
 Sugahara, Y., Ouchi, M., Harikane, Y., et al. 2019, *ApJ*, 886, 29
 Tonry, J., & Davis, M. 1979, *AJ*, 84, 1511
 Topping, M. W., Shapley, A. E., Reddy, N. A., et al. 2019, arXiv e-prints, arXiv:1912.10243
 Torrey, P., Vogelsberger, M., Marinacci, F., et al. 2019, *MNRAS*, 484, 5587
 Toshikawa, J., Uchiyama, H., Kashikawa, N., et al. 2018, *PASJ*, 70, S12
 Weinberg, D. H., Andrews, B. H., & Freudenburg, J. 2017, *ApJ*, 837, 183
 Wise, J. H., Demchenko, V. G., Halicek, M. T., et al. 2014, *MNRAS*, 442, 2560
 Zahid, H. J., Kudritzki, R.-P., Conroy, C., Andrews, B., & Ho, I. T. 2017, *ApJ*, 847, 18

Table 1
Summary of Objects Used

Name (1)	z (2)	M_{UV} (3)	Instrument (4)	T_{exp} (mins) (5)	Ref. (6)
J0215-0555	5.744 ± 0.006	-22.85	X-shooter	450	This work
			FOCAS	220	M16
J0210-0523	5.890 ± 0.006	-23.14	X-shooter	450	This work
			FOCAS	83	M16
J0219-0416	5.973 ± 0.006	-22.56	FOCAS	80	M16
J0857+0142	5.827 ± 0.006	-22.71	FOCAS	100	M16
J0210-0559	5.826 ± 0.005	-22.52	FOCAS	125	M16
J0848+0045	5.781 ± 0.004	-23.04	FOCAS	140	M16
J1628+4312	6.020 ± 0.008	-22.90	FOCAS	170	M18a
J1211-0118	$6.0293 \pm 0.0002^*$	-23.23	OSIRIS	60	M18a
J1630+4315	6.027 ± 0.008	-22.95	FOCAS	45	M18a
J2233+0124	6.004 ± 0.008	-22.52	FOCAS	60	M18a
J0212-0158	6.012 ± 0.006	-23.72	OSIRIS	60	M18a
J0218-0220	5.867 ± 0.015	-22.94	FOCAS	60	M18a
J0159-0359	5.781 ± 0.004	-22.78	FOCAS	60	M18a
J2237-0006	5.777 ± 0.005	-22.37	FOCAS	100	M18a
J1428+0159	6.006 ± 0.004	-24.30	OSIRIS	30	M18b
J0917-0056	6.006 ± 0.004	-23.60	OSIRIS	120	M18b
J0212-0315	5.916 ± 0.005	-22.85	FOCAS	50	M18b
J0212-0532	5.901 ± 0.005	-22.42	FOCAS	50	M18b
J2311-0050	5.904 ± 0.008	-22.72	FOCAS	50	M18b
J1609+5515	5.868 ± 0.008	-22.41	FOCAS	80	M18b
J1006+0300	5.863 ± 0.015	-22.98	FOCAS	45	M18b
J0914+0442	5.851 ± 0.006	-23.79	FOCAS	50	M18b
J0219-0132	5.780 ± 0.003	-22.25	FOCAS	30	M18b
J0915-0051	5.664 ± 0.006	-22.60	FOCAS	75	M18b
J135348.55-001026.5	6.176 ± 0.004	-24.76	OSIRIS	60	M19
J144216.08+423632.5	6.016 ± 0.015	-22.93	FOCAS	30	M19
J092117.65+030521.5	5.970 ± 0.011	-22.76	FOCAS	30	M19
J115755.51-001356.2	5.867 ± 0.007	-22.98	FOCAS	40	M19
J123841.97-011738.8	5.782 ± 0.004	-23.37	FOCAS	30	M19
J162657.22+431133.0	5.819 ± 0.003	-22.78	FOCAS	50	M19
J020649.98-020618.2	5.721 ± 0.013	-23.83	OSIRIS	60	M19

Note. — (1) Object Name. (2) Redshift. (3) Absolute UV magnitude. (4) Instrument. (5) Exposure time. (6) Reference (M16: Matsuoka et al. 2016, M18a: Matsuoka et al. 2018a, M18b: Matsuoka et al. 2018b, M19: Matsuoka et al. 2019).

*The systemic redshift of J1211-0118 is derived from ALMA observations in Harikane et al. (2019).

Table 2
Properties of Absorption and Emission Lines

Name	Ion	λ_{rest} (\AA)	I_0/C	FWHM (km s^{-1})	EW_0 (\AA)
(1)	(2)	(3)	(4)	(5)	(6)
Composite spectrum	Si II	1260.42	-0.6 ± 0.1	761 ± 241	-2.1 ± 0.5
	O I	1302.17	-0.4 ± 0.3	1483 ± 925	-2.7 ± 1.6
	Si II	1304.37	-0.4 ± 0.1	761 ± 241	-1.4 ± 0.6
	C II	1334.53	-0.8 ± 0.2	628 ± 193	-2.4 ± 0.5
	Si IV	1393.76	-0.5 ± 0.1	1189 ± 291	-3.1 ± 0.9
J0215–0555	Si IV	1402.77	-0.4 ± 0.1	1189 ± 291	-2.5 ± 0.6
	Si II	1260.42	-1.1 ± 0.6	1310 ± 517	-6.0 ± 2.9
	O I	1302.17	-0.9 ± 3.3	420 ± 453	-1.8 ± 2.7
	Si II	1304.37	-1.1 ± 2.3	1310 ± 517	-3.9 ± 4.5
	C II	1334.53	-1.1 ± 1.2	1000 ± 517	-4.5 ± 2.9
	Si IV	1393.76	-1.1 ± 3.0	998 ± 432	-4.7 ± 4.7
	Si IV	1402.77	-1.1 ± 1.8	998 ± 432	-5.2 ± 2.3
	C IV	1548.20	-0.9 ± 0.5	1192 ± 655	-5.1 ± 5.0
	C IV	1550.78	-0.9 ± 0.6	1192 ± 655	-5.6 ± 5.5
	He II	1640.42	< 0.5
	O III]	1660.81	< 0.5
	O III]	1666.15	< 0.5
	[C III]	1906.68	< 8.1
C III]	1908.73	< 0.9	
J0210–0523	Si II	1260.42	-0.7 ± 0.6	834 ± 361	-1.8 ± 3.1
	O I	1302.17	-1.1 ± 3.1	560 ± 482	-2.9 ± 2.9
	Si II	1304.37	-0.9 ± 1.9	834 ± 361	-3.4 ± 4.7
	C II	1334.53	-0.9 ± 0.2	948 ± 463	-3.8 ± 2.0
	Si IV	1393.76	-0.6 ± 1.3	623 ± 601	-1.7 ± 2.8
	Si IV	1402.77	-0.1 ± 0.6	623 ± 601	-0.6 ± 4.7
	C IV	1548.20	-0.8 ± 0.5	815 ± 640	-3.4 ± 4.1
	C IV	1550.78	-0.9 ± 0.4	815 ± 640	-3.0 ± 4.0
	He II	1640.42	< 0.5
	O III]	1660.81	< 0.8
	O III]	1666.15	< 0.4
	[C III]	1906.68	< 0.4
	C III]	1908.73	< 0.7

Note. — (1) Object Name. (2) Ion. (3) Rest-frame vacuum wavelength. (4) Amplitude of the line. (5) Width of the line corrected for the instrumental broadening. (6) Equivalent width of the line. The upper limit is 3σ . The upper limit of [C III]1907 in J0215–0555 is relatively weak because the wavelength of the line is contaminated by a night sky OH line.

Table 3
Measurements for $z \sim 6$ Galaxies

Name	z	M_{UV}	$\log(M_*/M_\odot)$	Max. abs. depth	$12 + \log(\text{O}/\text{H})$	Z_*/Z_\odot
(1)	(2)	(3)	(4)	(5)	(6)	(7)
$z \sim 6$ composite	5.868	–22.90	10.5	0.85 ± 0.16	$8.68_{-0.18}^{+0.15}$	$0.42_{-0.14}^{+0.28}$
J0215–0555	5.741	–22.85	10.5	> 0.40 (2σ)	$9.25_{-0.53}^{+0.43}$...
J0210–0523	5.890	–23.14	10.6	0.77 ± 0.45	$8.60_{-0.60}^{+0.46}$...

Note. — (1) Object Name. (2) Redshift. (3) Absolute UV magnitude. (4) Stellar mass estimated from the UV magnitude with the empirical relation in Song et al. (2016). (5) Maximum absorption depth. (6) Gas-phase metallicity. (7) Stellar metallicity